PAPER • **OPEN ACCESS**

Cryogenic ion trap system for high-fidelity near-field microwave-driven quantum logic

To cite this article: M A Weber *et al* 2024 *Quantum Sci. Technol.* **9** 015007

IOP Publishing Quantum Sci. Technol. 9 (2024) 015007 https://doi.org/10.1088/2058-9565/acfba8

Quantum Science and Technology

OPEN ACCESS

RECEIVED
25 November 2022

REVISED
23 May 2023

ACCEPTED FOR PUBLICATION
20 September 2023

PUBLISHED
25 October 2023

PAPER

Cryogenic ion trap system for high-fidelity near-field microwave-driven quantum logic

M A Weber*, C Löschnauer, J Wolf, M F Gely, R K Hanley, J F Goodwin, C J Ballance, T P Harty and D M Lucas

Department of Physics, Clarendon Laboratory, University of Oxford, Parks Road, Oxford OX1 3PU, United Kingdom
* Author to whom any correspondence should be addressed.

E-mail: marius.weber@oxionics.com

Keywords: ion-trap, quantum computing, quantum information, cryogenic, quantum entanglement, quantum information architectures, microwave

Supplementary material for this article is available online

Abstract

We report the design, fabrication, and characterization of a cryogenic ion trap system for the implementation of quantum logic driven by near-field microwaves. The trap incorporates an on-chip microwave resonator with an electrode geometry designed to null the microwave field component that couples directly to the qubit, while giving a large field gradient for driving entangling logic gates. We map the microwave field using a single $^{43}Ca^{+}$ ion, and measure the ion trapping lifetime and motional mode heating rates for one and two ions.

Trapped ions are a promising candidate for building a general-purpose quantum processor, with both single-qubit [1] and two-qubit [2–5] gates with the fidelities required for quantum error correction [6, 7]. Trapped-ion qubits are typically implemented using electric-dipole-forbidden transitions where the state lifetime is sufficiently long that decoherence via spontaneous emission is negligible, leading to coherence times of the order of minutes [8–10] or longer [11]. The qubit transitions typically lie in the optical domain operating on electric-quadrupole transitions [12], or in the microwave domain between hyperfine states within the same manifold [13]. Although hyperfine qubits lie in the microwave domain, they are usually manipulated using stimulated Raman transitions with tightly focused laser beams, as the short optical wavelength enables single-qubit addressing [14] and efficient coupling between the ions' spin and motional degrees of freedom [15]. Laser-driven operations utilising stimulated Raman transitions fundamentally suffer infidelity arising from photon scattering [16–18]. Furthermore, the scaling of stimulated Raman operations to a large-scale quantum processor is challenging as many high-intensity laser beams need to be controlled and aligned with sub-μm precision.

Microwave radiation can be used to drive hyperfine or Zeeman qubits directly [15]. However, as the free-space wavelength of microwave radiation is much greater than that of laser light, free space spatial selectivity and spin-motion coupling of microwave radiation is impractical. The spatial selectivity [19] and spin-motion coupling can be increased by several orders of magnitude if one is able to engineer a large spatial gradient in the microwave field. One way to achieve an effective microwave field gradient is by combining far-field microwaves with a strong, static magnetic field gradient [20–22]. However, this method requires radiative atomic-dressing techniques [23–25] to minimise decoherence because the qubit states need to be first-order sensitive to magnetic fields. An alternative solution is to position the ions in the near-field regime of a microwave-current-carrying conductor [15, 26, 27]; here the field gradient is determined by the distance to the conductor and conductor geometry rather than the free-space wavelength of the microwaves. In addition to these methods, a novel spin-motion coupling has been recently demonstrated using a radio-frequency field gradient oscillating close to the ions' motional frequency [28].

Microwave technology is more mature than laser technology, and is used in many everyday devices such as mobile telephony. It is commercially available at lower cost than laser systems, and is also easier to control. Microwave circuitry can also be directly integrated into ion trap structures, which facilitates the production of chip-based ion traps that are amenable to scaling into quantum 'CCD-like' devices [15, 29–32]. There have

been significant advances in recent years using surface traps with single-layer [27, 33, 34] and multi-layer [35, 36] integrated microwave circuit elements to perform quantum logic gates, with the highest-fidelity two-qubit operations [4, 37, 38] approaching the fidelities of state-of-the-art laser-based systems [2, 3, 5].

This paper details the design, construction, and characterisation of a surface-electrode trap with integrated microwave circuitry, which is designed for implementing microwave-driven two-qubit gates with significantly improved fidelity and/or speed compared with that achieved in our first-generation system (gate fidelity of 0.997 with a duration of 3.25 ms) [37]. The apparatus features a surface trap with a novel microwave electrode concept, designed for a previously unused hyperfine 'atomic clock' qubit [8, 10] in $^{43}Ca^{+}$, operating at a static magnetic field of $B_0 \approx 288$ G. The surface trap is designed to operate at cryogenic temperatures to offset increased motional mode heating (from the reduced ion height), to reduce ion loss from background gas collisions, and to increase the achievable microwave field gradient (from more favourable electric losses and power handling). For the purpose of characterizing performance, the system is designed to operate at any temperature from cryogenic (∼20 K) to ambient (300 K).

The remainder of this paper is structured as follows. In section 1 we outline the desired improvements relative to our first-generation experiment [37], before describing the design and fabrication of the surface trap in sections 2 and 3. We detail in sections 4 and 5 the construction of the experimental apparatus which enables the surface trap to be operated at cryogenic temperature $T \sim 20$ K. In section 6 we present characterisation measurements of the surface trap and discuss the future prospects for high-speed and high-fidelity microwave-driven quantum logic in this system.

1. Targeted improvements

The experiment targets improvements to the two-qubit gate speed and fidelity by employing an improved trap design and choice of qubit. A particular focus is placed on gate speed improvements as several error sources for entangling gates increase with the gate duration [3].

In the near-field regime of a microwave-current-carrying conductor, the spin-motion coupling strength is proportional to the spatial gradient of the microwave magnetic field. Therefore, the two-qubit gate speed can be improved by increasing this magnetic field gradient. Naively, this can be achieved by increasing the microwave power $P_{\mu W}$ injected into the conductor. However, a power increase is not a practical solution as the field gradient scales as $\sqrt{P_{\mu W}}$, leading to quadratic scaling of input power and trap power-handling requirements for a linear increase in gate speed. A more efficient approach is to reduce the ion-to-electrode distance d, as the field gradient scales as $\sim 1/d^2$. A disadvantage of the reduced ion-to-electrode distance is the likely increase in electric field noise, which has been observed to scale approximately as $\sim 1/d^4$ [39–41]. Greater electric field noise increases two-qubit gate errors and therefore needs to be balanced against any gain from an increased gate speed. To mitigate the field noise, one can cool the trap electrodes to cryogenic temperatures; this technique has been shown to reduce electric field noise by several orders of magnitude [39, 41–43].

The two-qubit gate fidelity can also be improved by increasing the ratio of microwave field gradient to field amplitude. The field gradient drives the two-qubit gate, whilst the field amplitude leads to unwanted AC Zeeman shifts, and can drive undesired magnetic dipole transitions. One could interfere fields from multiple independent microwave electrodes to produce a large field gradient while achieving cancellation between the microwave amplitude of the electrodes, a microwave-null [26]. However, in practice the active stabilisation of all microwave current amplitudes and phases with sufficient accuracy in multiple electrodes is an additional complication. An alternative approach is to design a trap which creates a microwave null passively [34], eliminating technical differential amplitude and phase noise.

As well as the trap design considerations above, we aim to improve the gate speed and fidelity through a more favourable choice of qubit states than in our previous work [37]. In that experiment, we employed a $|\Delta m| = 1$ qubit transition. Such a transition can be driven by a linearly-polarised microwave field oriented orthogonal to the quantisation axis. This field creates an equal superposition of left- and right-circularly polarised fields, hence only half the applied microwave power is available to drive the qubit transition. It is therefore beneficial to utilise a $\Delta m = 0$ qubit transition where all of the available microwave field gradient can be used to drive the spin-motion coupling.

We previously used the 'clock' qubit states $|F = 4, m = 0\rangle$ and $|F = 3, m = +1\rangle$ in the $4S_{1/2}$ ground level hyperfine manifold of $^{43}Ca^{+}$ (figure 1), operating at a static field of $B_0 \approx 146$ G, where the $|\Delta m| = 1$ qubit transition energy is first-order insensitive to magnetic field fluctuations [1]. In this second-generation experiment, we use a $\Delta m = 0$ clock qubit operating on the $|F = 4, m = +1\rangle \leftrightarrow |F = 3, m = +1\rangle$ transition at $B_0 = 287.783$ G, allowing efficient coupling of the available microwave gradient to drive the entangling operation. In addition to the efficient microwave gradient polarisation, the intrinsic transition strength of the $\Delta m = 0$ qubit is $\approx\sqrt{2}$ larger than that of the $|\Delta m| = 1$ qubit. Together, these factors increase the

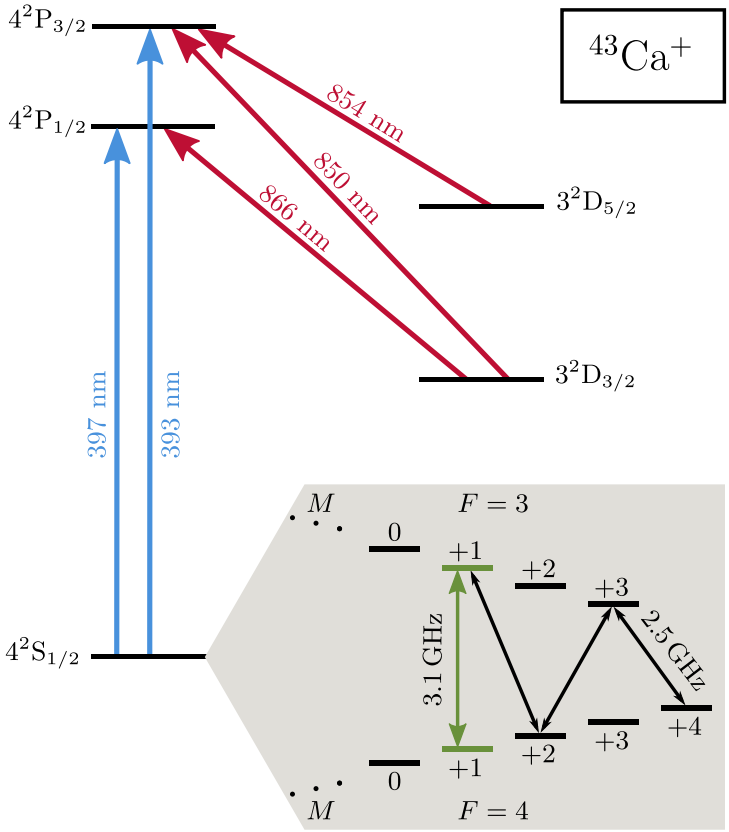

Figure 1. Energy level diagram of $^{43}Ca^{+}$ showing the relevant transitions for laser cooling, state preparation, and readout. The lower panel shows relevant states within the hyperfine structure of the $4^2S_{1/2}$ ground level, at a static magnetic field of $B_0 = 287.783$ G. The green states show the clock transition used for the qubit in this work, and the black arrows show the transitions used for state preparation and readout. Zeeman splittings between adjacent m states are ≈110 MHz.

achievable two-qubit operation speed by a factor of ≈2 for a given microwave power. Alternatively, when operating at the same gate speed, AC Zeeman shifts and driving of undesired spectator transitions are reduced. The increase in the static magnetic field from 146 G to 288 G approximately doubles the detuning of spectator transitions from the qubit transition, further suppressing their effects.

In addition to the change of qubit, the ion-to-electrode distance in this new surface trap is $d = 40\,\mu$m, approximately half that of the previous trap. This increases the achievable microwave field gradient and hence the two-qubit gate speed by an additional factor ∼4 and is complemented by an electrode layout which gives a passive microwave null. To mitigate the anticipated increase in the motional mode heating rate $\dot{\bar{n}}$ due to smaller d, the surface trap is designed to operate at cryogenic temperatures. An added benefit of cryogenic operation is the vacuum improvement, giving fewer background gas collisions and longer ion trapping lifetime.

Cryogenic operation also reduces resistive losses within the microwave electrode, leading to higher achievable microwave currents and thus field gradients. Note however that at microwave frequencies, the electrode resistance R will not scale linearly with the gold resistivity ρ. Indeed, since skin depth also reduces with the square-root of resistivity, electrode resistance will follow $R \propto \sqrt{\rho}$.

2. Surface trap design

The use of symmetry to passively null the field amplitude eliminates the need for calibration and potential stabilisation of multiple microwave signals, reducing potential sources of gate error. A 'meander' electrode structure has previously been shown to passively null the microwave field in all three spatial axes [34, 44]. The position of the minimum relies on a complex interference pattern between multiple sections of the electrode, making the surface trap design sensitive to the geometry and microwave current distribution. This is particularly problematic for designs relying on a single metal layer, where the ground plane is effectively bisected by the meander and radio frequency (RF) electrodes. The design of a meander trap that aims to minimise the field amplitude but maximise the field gradient is therefore difficult as the optimisation is multi-dimensional and not constrained by symmetries, leading to difficulties finding a broad global

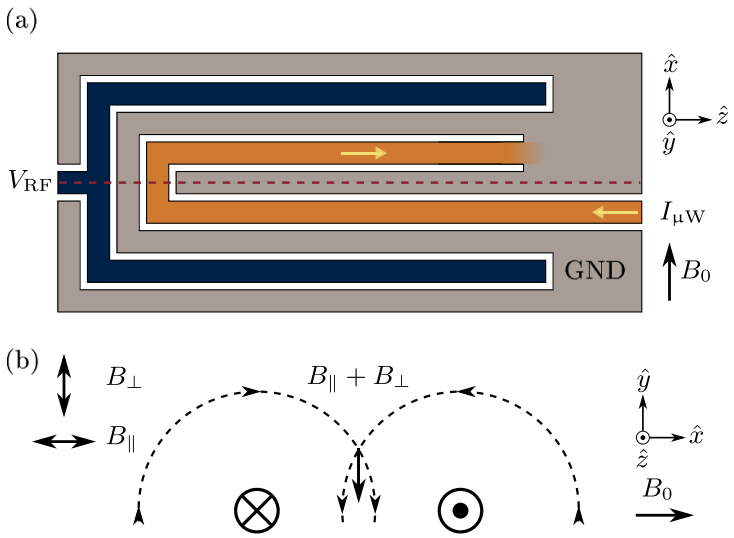

Figure 2. (a) Simplified top view of the surface trap (not to scale), illustrating the operational principles. The blue, orange, and grey regions correspond to the RF, microwave, and ground plane electrodes respectively. The red dashed line shows the position of the RF null, and B_0 is the applied static magnetic field. (b) A cross-sectional view of the instantaneous magnetic field created by current flowing in the microwave electrodes (shown as one-dimensional wires for illustration).

minimum. Furthermore, as the meander passively nulls the microwave field along all axes, it has the undesirable side-effect of restricting the achievable Rabi frequency used for state preparation. An additional microwave electrode can be added outside the meander [44]; however the microwave field produced by such an electrode is heavily screened by nearby induced currents, resulting in a weak field at the trap centre and hence slow state preparation.

To address the challenges associated with the meander design, we have designed a surface trap using a single, resonantly-coupled 'U-shaped' microwave electrode (see figure 2(a)) which is terminated on the surface trap ground plane to form a quarter-wave ($\lambda/4$) resonator [45]. The 'U-shaped' microwave electrode design only results in a passive microwave field null along a single axis, thereby allowing for faster state preparation. Further, the resonant structure allows for efficient coupling of microwave currents onto the surface trap. A $\lambda/4$ resonator was chosen over a $\lambda/2$ resonator as the shorter microwave electrode length limits resistive losses. Additionally, a $\lambda/4$ resonator allows the microwave electrode to be grounded, hence avoiding photoelectric charging effects. The inherent symmetry of the 'U-shaped' microwave electrode reduces the number of free parameters in the optimisation of a microwave minimum, making global optimisation more feasible. The symmetry also increases the robustness of the trap to manufacturing imperfections, such as a global reduction in electrode width, as only asymmetric imperfections break the symmetry.

The basic design concept is illustrated in figure 2(b), where we consider a cross-sectional view of the current in the microwave electrode at a single instant in time. Along the symmetry axis the magnetic field components parallel to $\hat{x}$ destructively interfere, resulting in a field null. As one moves closer to either section of the electrode, the field component B_x increases. With the static magnetic field parallel to $\hat{x}$, the required π-polarised field gradient is created, while the π-field that couples directly to the qubit is nulled. In reality, a small phase difference in the two opposing currents results in a minimum instead of a perfect null (see section S2 A). Along $\hat{y}$ the fields constructively interfere, resulting in a non-zero field component B_y which facilitates a large Rabi frequency to drive both σ^+ and σ^- transitions for state preparation in the hyperfine manifold without the need for additional electrodes. The presence of such a large σ-field component which does not couple to the qubit may appear detrimental to the entangling operation; however we have shown in our previous work that this is not the limiting source of infidelity [37]. Note that the 'hairpin turn' of the microwave electrode is located 15 times further than the smallest ion-electrode distance and therefore does not significantly contribute to the field.

The microwave electrode was designed to be a resonant structure with a modest Q-factor ($Q_{\mathrm{tot}} \approx 10$, see section S3), with a centre frequency of 3.1 GHz to match the hyperfine splitting of the $|F=4, m=+1\rangle \leftrightarrow |F=3, m=+1\rangle$ transition at $B_0 = 288\,\mathrm{G}$. The Q-factor was chosen to be large enough to increase the achievable field gradient at the ion position, but low enough to obtain a large microwave bandwidth, which enables state preparation in the hyperfine manifold where the most distant frequency is that of the $|F=4, m=+4\rangle \leftrightarrow |F=3, m=+3\rangle$ transition at $\approx$2.5 GHz. The geometry of the microwave

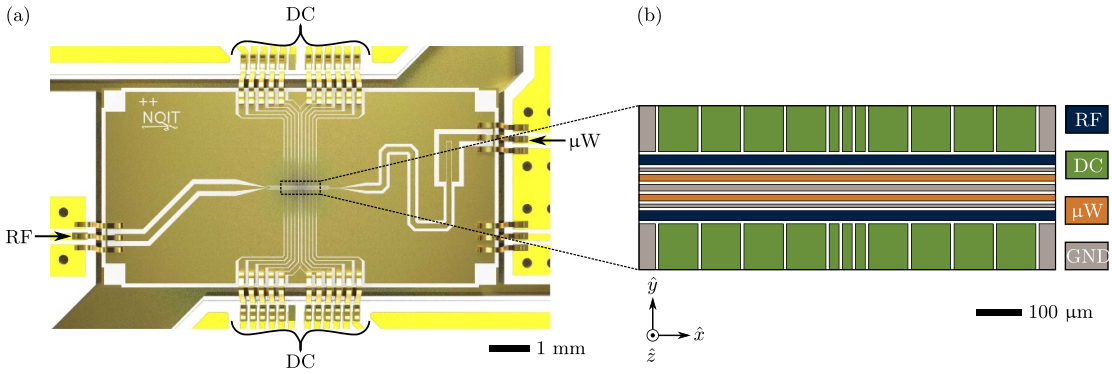

Figure 3. (a) Rendered image of the surface trap detailing the electrical connections for the radio frequency (RF), DC, and microwave (μW) electrodes. The meander path for the microwave line allows sufficient length to form the quarter-wave resonator. (b) Enlarged scale view of the central trapping region, showing the structure of the DC electrodes.

Table 1. The designed and measured widths of electrodes on the optimised surface trap.

Electrode	Design (μm)	Measured (μm)
Dielectric gap	4.5	5.2
Microwave electrode	8.5	7.8
RF electrode	18.8	18.4
Wide DC electrode	85.5	85.3
Narrow DC electrode	25.5	25.0
Inner ground	9.5	8.8
Outer ground	5.5	4.8

Table 2. Simulated microwave field gradient, and field amplitude parallel and perpendicular to the quantisation axis defined by $\boldsymbol{B_0}$ at the RF null for an input microwave power of 1 W. For a perfectly symmetric design, we would have $B^0_{\parallel} = 0$; the imperfect nulling of $B^0_{\parallel}$ is useful in practice for driving the qubit carrier transition.

Temperature	$\partial B_{\parallel}/\partial x$ (T/m)	$B^0_{\parallel}$ (μT)	$B^0_{\perp}$ (μT)
300 K	26	39	462
20 K	72	108	1282

electrode was optimised to maximise the microwave field gradient whilst minimising the microwave field strength at the position of the RF null, where the ion is trapped. The microwave fields were simulated using finite-element analysis software [46, 47] (see section S1), as at microwave frequencies the proximity of other conductors leads to a complex distribution of currents which cannot be solved analytically. The microwave electrode is placed between the two arms of the RF electrode, as shown in figure 2, and is surrounded by ground planes to reduce coupling between sections of the microwave electrode.

A rendered image of the optimised surface trap design is shown in figure 3(a), and its central trapping region is detailed in figure 3(b). The widths of the electrodes shown in the central trapping region are given in table 1. The microwave electrode path to the trap region was chosen to ensure the correct length to form the $\lambda/4$ resonator. The trapping region has 22 DC electrodes in total, 11 per side, where the central 3 electrode pairs are narrower to facilitate splitting of ion chains.

Microwave power is delivered through a 50 Ω feedline to provide good impedance matching to the microwave source. This feedline is capacitively coupled to the microwave electrode to inhibit DC coupling to the electrode. Inevitably, this coupling capacitor also allows microwave energy to leak out of the resonator, reducing the total quality factor of the resonator. We utilize this fact to limit the quality factor (overcoupling the resonator) at cryogenic temperatures. With our expected residual resistivity ratio (RRR) of 15 [48], the quality factor would change from ∼8 at room temperature to ∼120 (linewidth ∼50 MHz) at cryogenic temperatures if only determined by metal resistivity. The chosen capacitance to the feedline limits the total quality factor to $Q_{\text{tot}} < 17$.

The magnetic field components produced by the optimised microwave electrode design, both at room and cryogenic ($T = 20$ K) temperatures, are detailed in table 2 and figure 4. The figure shows the simulated magnetic field parallel $B_{\parallel}$ and perpendicular $B_{\perp}$ to the quantisation axis produced by the microwave electrode at 3.1 GHz for an input power of 1 W. The upper plot shows a 2D plane above the trapping region,

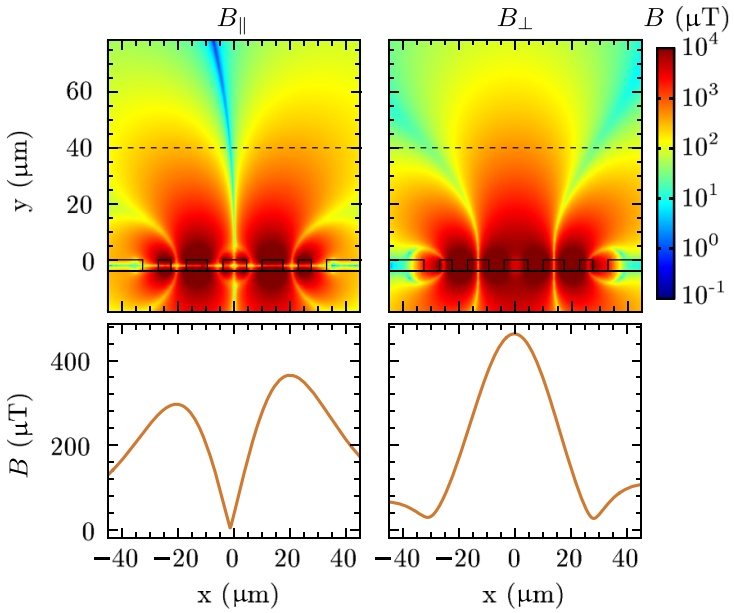

Figure 4. Simulated room-temperature magnetic field components parallel $B_{\parallel}$ and perpendicular $B_{\perp}$ to the atomic quantisation axis produced by the microwave electrode at 3.1 GHz for an input power of 1 W. The upper figures show the magnetic field in a 2D plane above the surface trap ($y = 0$), and the lower figures show a slice at the ion trapping height of $y = d = 40\,\mu$m, where $(x = 0, y = 40)\,\mu$m is the position of the trapping RF null.

and the lower plots show a transect at the ion trapping height of $d = 40\,\mu$m. The simulations show that we are able to create a minimum in $B_{\parallel}$, as expected from the simplified model shown in figure 2. Note that the minimum of the magnetic field is displaced slightly from the RF null ($x = 0$) due to the asymmetry in the current amplitude on either side of the ion, resulting in a small residual magnetic field amplitude which couples to the clock qubit (see section S2 A). This does however enable the application of a carrier tone which can be used to implement the two-qubit dynamically-decoupled Mølmer–Sørensen gate [37, 49, 50] and single-qubit rotations.

The quantities calculated at cryogenic temperature assume knowledge of the RRR, which characterizes the change in resistance of the gold trap top-layer (see section 3) between room and cryogenic temperatures. The RRR depends strongly on the purity of the gold [51], as well as on the deposition methods. The value quoted above, RRR= 15, used in simulation and design of the device, is at best an educated guess. The impact of the uncertain RRR value is mitigated by the relatively large coupling capacitance which is expected to dominate the resonator losses at cryogenic temperatures.

3. Surface trap fabrication

The surface trap was constructed from a 430 μm thick, high-purity (99.996%), mono-crystalline sapphire wafer onto which layers of Ti (40 nm), Pt (60 nm), and Au (100 nm) were sequentially deposited using electron-beam evaporation. A sapphire substrate was chosen for its low loss tangent and excellent thermal conductivity at cryogenic temperatures. The Ti creates an adhesion layer and the Au provides a chemically passive surface finish. At the elevated temperatures used to bond the surface trap to the cryogenically-cooled pillbox (see section 5), the Ti would start to diffuse into the Au layer [52]; the Pt layer acts as a diffusion barrier between the Ti and Au surfaces [53], ensuring a pure Au finish. To create the surface trap electrodes, a 6 μm photo-resist was applied to the top side, and then selectively exposed to UV light through a mask. Photo-resist which was exposed to the UV light was removed, after which a layer of Au was electroplated onto the surface trap (see [54] for details of the electroplating process). The Au layer was chosen to be 4 μm thick as this is several times thicker than the room temperature skin depth of 1.35 μm at 3.1 GHz. The remaining photo-resist was then also removed, and the metallic layers beneath the photo-resist were removed using argon-ion milling, revealing the finished surface trap. Approximately 64 trap chips were made on the same 3" sapphire wafer, with some design variations (for example, with a range of microwave resonator lengths so that the chip whose resonator most closely matched the qubit frequency could be selected); the wafer was diced into individual chips.

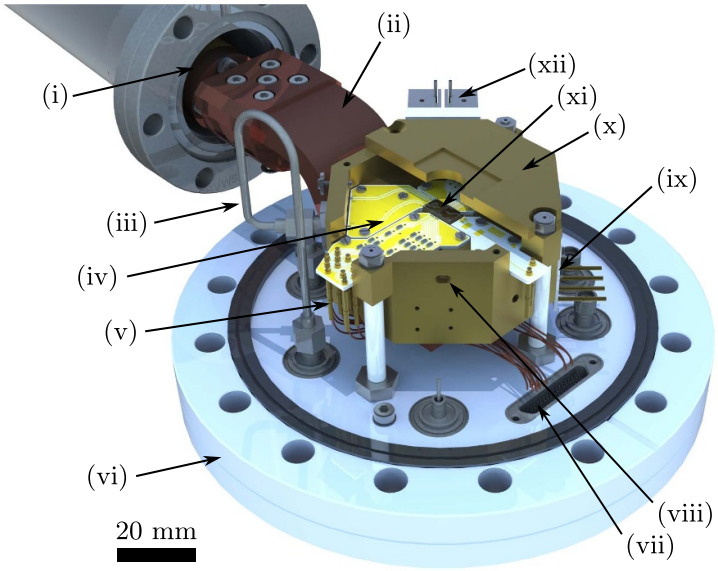

Figure 5. Rendered image of the vacuum chamber. Labelling is as follows: (i) LHe flow cryostat head; (ii) thermal strap; (iii) microwave semi-rigid coaxial cable; (iv) microwave PCB; (v) DC electrode connections; (vi) CF100 base flange; (vii) 51 pin micro-D feedthrough; (viii) optical access holes; (ix) temperature sensor; (x) pillbox lid (cut away for illustration); (xi) surface trap chip; (xii) atomic ovens [60].

4. Filter boards

The surface trap was electrically connected via gold wire-bonds to several printed-circuit boards (PCBs). These PCBs were manufactured on alumina substrates (96% purity), with 60 μm copper traces, coated with a $\sim$100 nm layer of electroless palladium autocatalytic gold (EPAG). Alumina has good thermal conductivity and low loss tangent, and EPAG provides a nickel-free, gold surface finish which facilitates Au-Au wire-bonding. The undersides of the PCBs were also EPAG coated to provide a ground plane connection to the pillbox (figure 5). All electrical components on the PCBs were soldered using SAC305 solder as it is non-magnetic and ultra-high-vacuum (UHV) compatible. UHV compatible flux [55] was also used to improve the quality of solder joints.

There are five PCBs in total: two DC PCBs, a microwave PCB, an RF PCB, and a temperature sensor PCB. The two DC PCBs are used to simplify routing around the RF and microwave signals which are injected from opposing sides of the trap. Each DC PCB contains eleven separate traces with an integrated single-pole RC filter ($R = 1\,k\Omega, C = 1\,nF, f_c = 160\,kHz$) on each trace. The cut-off frequency f_c was chosen to be significantly lower than the typical secular frequencies of trapped ions (several MHz), but high enough to permit rapid ion transport operations. The RF and microwave PCBs are both singular, grounded coplanar waveguides which were designed to be 50 Ω impedance-matched at their respective frequencies. Both of these PCBs have multiple vias between the top and bottom ground planes, close to the waveguides to reduce the propagation of parasitic modes. The RF PCB also contains a $\sim$1 nH inductive choke in series which was intended to reduce undesired microwave coupling into the RF wiring. Finally, the temperature sensor PCB contains a Kelvin-connected resistance temperature detector (RTD), and is mounted on the side of the pillbox (figure 5).

5. Cryogenic design

There have been multiple studies [39, 42, 43, 56, 57] showing the benefits of operating ion traps at cryogenic temperatures. The data displayed in [43] suggests that cooling from room temperature to $T\sim$20 K reduces the motional heating rate $\dot{\bar{n}}$ by nearly two orders of magnitude (with only a factor $\sim$2 further reduction available by cooling further to $T \sim 4$ K). Furthermore, cryogenic pumping leads to extremely low background-gas pressures, which can reduce the trapped ion loss rate to negligible levels [58, 59]. In addition to these benefits, the cryogenic temperature reduces the resistive losses in the microwave electrode and thus increases the quality factor of the resonator, leading to a larger field gradient for a given input power. The thermal conductivity of sapphire is maximal near 20 K, allowing efficient transfer of heat from the microwave electrode to the pillbox.

Table 3. Expected heat load on the pillbox via vacuum chamber components and radiative transfer. SS, OFC and PTFE stand for stainless steel, oxygen-free copper and polytetrafluoroethylene respectively. The total expected heat load is indicated in bold. Notably, the heat load is dominated by conduction through the short support legs. The length of these supports is limited by space constraints.

Source	Material	Heat load (W)
Support legs	316 stainless steel	1.43
DC wires	BeCu	0.18
RF and GND wires	BeCu	0.08
RTD wires	BeCu	0.04
Microwave coax	SS/OFC/PTFE/Ag	0.13
Radiative	—	0.15
	Total	**2.01**

There are two main challenges when designing a cryogenically-cooled apparatus. Firstly, the surface trap must be sufficiently thermally isolated from its surrounding room temperature vacuum chamber that it can be effectively cooled with reasonable power, whilst still maintaining good optical access and electrical connections. Secondly, one must minimize vibrations of the trap (with respect to the optical beam-delivery components) induced by the cryostat.

There are many possible cryostat designs which can be used. We opted for a Janis ST-400 continuous-flow cryostat which does not require a complex vibration isolation stage. The apparatus design was optimised to reduce the passive heat load, whilst ensuring an excellent thermal contact between the surface trap and the cryostat. A thermal budget of the system is shown in table 3 [54]. Figure 5 shows a rendered image of the base flange of the vacuum chamber and the cryostat. At the centre of the vacuum chamber sits an oxygen-free high-conductivity copper pillbox mounted on three thin-walled (0.24 mm) stainless steel legs. The surface trap and relevant PCBs are mounted inside the pillbox. The pillbox provides a strong mechanical structure and large thermal mass for the surface trap. Larger thermal mass is desirable when to suppress intra-pulse thermal transients when applying high power microwave pulses. The pillbox also creates a low pressure (cryo-pumped) environment around the surface trap when operating at cryogenic temperatures, providing an enhancement in ion lifetime.

The pillbox was electroplated with a $\sim 5\,\mu$m layer of Au to reduce the absorption of black-body radiation, as well as to improve the bonding of the surface trap to the pillbox. The surface trap was bonded to the centre of the pillbox using eutectic bonding. A eutectic bonding process was chosen over other epoxy methods as the thermal conductivity of available epoxies can become a bottleneck in the thermalisation between the surface trap and pillbox. We soldered the surface trap to the pillbox using a 25 μm thick eutectic solder sheet with a composition of 80% Au and 20% Sn. This bonding process was performed *in vacuo* to mitigate oxides forming on the surface trap, at a temperature of $\sim 300\,^{\circ}$C [61]. A constant pressure of 0.5 MPa was applied to the surface trap during the bonding process to ensure a mechanically reliable bond. The PCBs were screw-mounted to the pillbox and electrical connections were made to the base flange. The DC and RF connections were made using push-fit crimp pins and 100 mm long BeCu wire, the latter used to minimise thermal conductivity. DC wire diameters are 0.321 mm whereas RF and ground wire diameters are 0.81 mm. The microwave connection was made using a UHV-compatible semi-rigid coaxial cable.

Optical access for laser beams is provided by 1.25 mm holes cut into the side faces of the pillbox. The diameter of the holes was minimised to reduce the vacuum conductance. This leverages the differential pumping at cryogenic temperatures to improve the vacuum quality experienced by the ion. These holes may also be used to aid laser beam alignment. A larger diameter hole in the pillbox lid allows collection of ion fluorescence with a numerical aperture of up to NA$= 0.6$. The atomic source is a short response-time resistively-heated oven [60]. This is mechanically isolated from the pillbox to ensure minimal thermal coupling. The temperature of the pillbox is measured using a Kelvin-connected RTD [62] mounted to the side of the pillbox. An RTD was chosen over a temperature diode as rectification of RF or microwave signals can lead to systematic shifts in the temperature measurement.

On cooling to cryogenic temperatures, the cryostat cold head contracts by ~ 0.9 mm. To ensure that the trap is mechanically decoupled from this contraction, the pillbox is connected to the cryostat head using a 60 mm long, S-shaped thermal strap [63]. The thermal strap is constructed from 205 sheets of 25 μm-thick copper foil, providing a flexible thermal connection with a measured room temperature conductivity of $0.80 \pm 0.05\,\mathrm{W\,K^{-1}}$. The surface trap moves a horizontal distance $<10\,\mu$m when cooled from room temperature to $T = 20$ K, relative to the laser beam positions, demonstrating the effectiveness of this mechanical isolation.

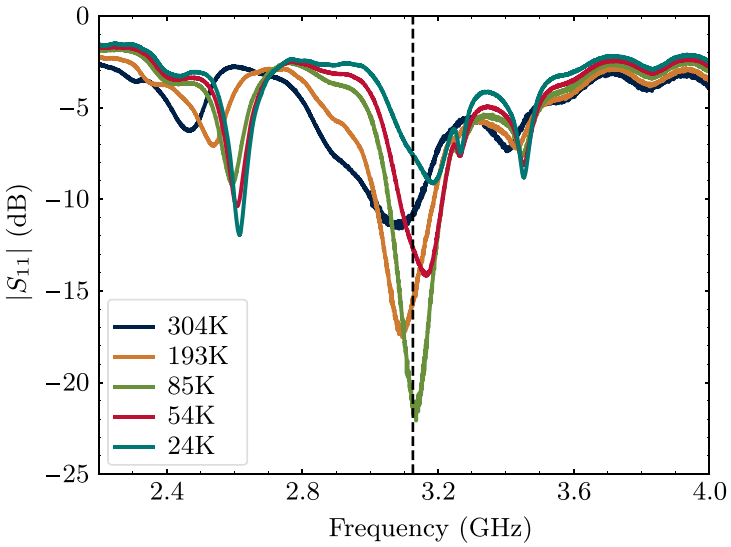

Figure 6. Measured S_{11} parameter of the microwave electrode as a function of trap temperature. The vertical dashed-dotted line shows the clock-qubit frequency at $|\mathbf{B}_0| = 288\,\mathrm{G}$.

6. Experimental characterization

6.1. Electrical measurements of trap chip

A vector network analyser was used to measure the power reflection (S_{11} parameter) of the microwave electrode as a function of trap temperature. Results are shown in figure 6. We observe a broad resonance, which is centred on the qubit frequency at cryogenic temperatures. We fabricated traps with a variety of resonator lengths, and chose the length that minimized the $|S_{11}|$ parameter at the qubit frequency at cryogenic temperatures. The modest quality factor Q of the resonance at room temperature allows the use of the trap without cryogenics, even though the resonant frequency is detuned from the qubit frequency. Other resonances are also observed, which we attribute to coupling between the microwave and RF electrodes (see section S2).

There are several characteristic features which change as a function of trap temperature. The first is the depth of the observed resonance, which is characterised by the quality factor Q. In this microwave resonator, the internal quality factor Q_{int} is mostly determined by resistive losses in the resonant structure, and the external quality factor Q_{ext} is determined by the capacitive coupling of the microwave resonator to the feedline [64]. Together these give the overall quality factor Q via $Q^{-1} = Q_{\mathrm{ext}}^{-1} + Q_{\mathrm{int}}^{-1}$. As the trap is cooled, the resistance of the gold decreases, which reduces resistive loss of the microwave resonator and hence increases Q_{int}. Q_{ext} is approximately constant, as the coupling across the gap between the feedline and the microwave resonator is defined by their on-chip geometry [65]. At room temperature, the microwave resonator is under-coupled to the feedline ($Q_{\mathrm{ext}} > Q_{\mathrm{int}}$). In this regime, the microwave current which is sent to the microwave electrode will mostly be reflected off the resonator, leading to a loss of power which could potentially have entered the resonator. As the trap is cooled to ∼20 K, the microwave resonator becomes critically-coupled to the feedline ($Q_{\mathrm{int}} = Q_{\mathrm{ext}}$), and we observe the smallest $|S_{11}|$ and maximum power transfer to the resonator. As the trap is cooled further, the microwave electrode becomes over-coupled ($Q_{\mathrm{ext}} < Q_{\mathrm{int}}$), and we observe an increase in $|S_{11}|$. Intuitively, when $Q_{\mathrm{ext}} < Q_{\mathrm{int}}$, too much energy will be leaking out of the microwave resonator into the feedline, damping the resonator and reducing the amplitude within it. It is challenging to design a critically-coupled resonator at a given temperature due to the unknown resistance of the gold prior to fabrication. To optimize the microwave current per unit input power for operation around 20 K, we would have to increase the external quality factor, by reducing the capacitance between the resonator and the feedline.

Another noticeable change is the shift in frequency of the microwave resonance, to which there are two main contributions. The dielectric constant of the sapphire changes by approximately 1.5% between room temperature and liquid helium temperatures [66]. This leads to a small change in the in-coupling capacitance as well as to an effective length reduction of the microwave resonator. The reduction in the gold resistance also contributes to a frequency shift of the resonance (see section S3).

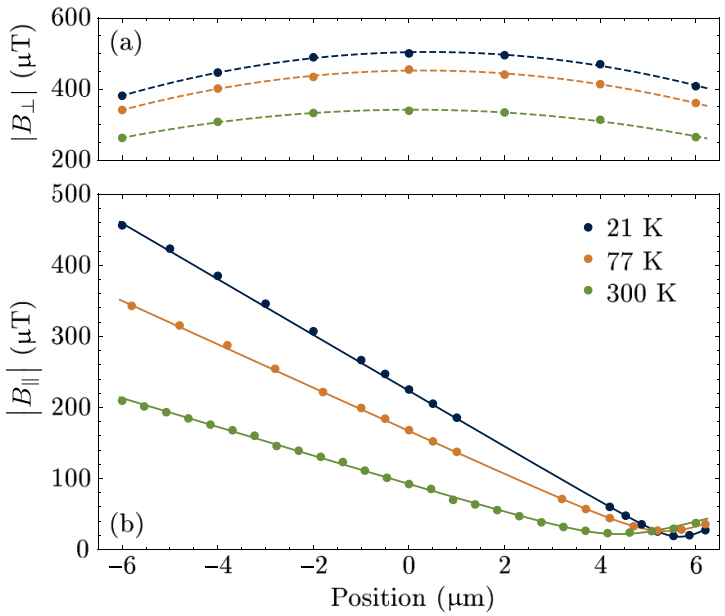

Figure 7. Microwave field measured with a single ion, for field amplitude (a) perpendicular $B_\perp$ and (b) parallel $B_\parallel$ to the static field B_0, at trap temperatures of $T = 300$ K, 77 K, and 21 K (green, orange, blue symbols respectively). The measured microwave field amplitude is normalised to an input power of 1 W. The dashed lines in (a) are guides to the eye, while the solid lines in (b) are fits to the data using equation (1). The trap centre (RF null) is at $x = 0$.

6.2. Microwave field measurements

The microwave-frequency magnetic field produced above the trap chip by the microwave resonator was measured using a single $^{43}Ca^+$ ion. Ions were loaded into the trap using isotope-selective photo-ionisation [67] from an isotopically enriched source (30%$^{43}Ca^+$, 70%$^{40}Ca^+$). The trapping RF was supplied at a frequency of 61.3 MHz and amplified to a voltage of ≈80 V using a series $L-C$ circuit, producing a radial secular frequency of ≈5.5 MHz, and radial trap depth of ∼30 meV. The axial secular frequency of 1.1 MHz was controlled via application of voltages to the DC electrodes. The DC electrodes were also used to break the degeneracy of the radial modes by ∼0.3 MHz and to tilt the radial mode angles by 15° to the trap plane, enabling efficient laser cooling with a single laser beam. Real-time experimental control was provided by modules from the ARTIQ/Sinara open-source ecosystem [68].

Measurements of the microwave field amplitude parallel and perpendicular to the quantisation axis provided by the 288 G static magnetic field were made by measuring the Rabi frequency on the $|F = 3, m = +1\rangle \rightarrow |F = 4, m = +1\rangle$ and $|F = 3, m = +1\rangle \rightarrow |F = 4, m = +2\rangle$ transitions respectively. The ion was initially laser cooled using counter-propagating 397 nm and 866 nm laser beams using techniques similar to those in [69], after which it was prepared in the $|F = 4, m = +4\rangle$ state via optical pumping with a circularly-polarised 397 nm beam propagating parallel to the static magnetic field. The ion was subsequently prepared in the $|F = 3, m = +1\rangle$ state using a series of microwave π-pulses (see figure 1). Rabi flopping was then driven on the transition of choice, after which microwave pulses transferred population in the $|F = 3, m = +1\rangle$ state back to the $|F = 4, m = +4\rangle$ state. Population in the $|F = 4, m = +4\rangle$ state was shelved in the metastable $3D_{5/2}$ level using 393 nm and 850 nm laser pulses [70]. The Doppler cooling beams were then applied and the state of the ion inferred by the absence or presence of ion fluorescence. Finally, the ion was repumped to the ground level using an 854 nm pulse.

To measure the microwave field amplitude as a function of $\hat{x}$, we varied the ion position by adjusting the trap DC voltages. The measured spatial distribution is shown in figure 7, at trap temperatures of $T = 300$ K, 77 K, and 21 K. As discussed previously, one expects a minimum in the component of the microwave field parallel to the static magnetic field (see figure 2(b)), resulting in a microwave field with a large gradient but small amplitude. As expected, we observe a minimum in this microwave component; however, this minimum is offset by several microns from the RF null. Consequently, the parallel microwave amplitude component $B_\parallel$ at the trap centre is larger than designed. Through further simulations and measurements, we deduced that this is caused by a resonant coupling between the microwave and RF electrodes (see section S2), due to an impedance mismatch at a boundary formed by the RF choke, its large solder pads, and the ∼200 Ω

Table 4. Measured microwave field gradient along the $\hat{x}$ direction, and field amplitude at the RF null, at different trap temperatures with a microwave input power of 1 W, for the $B_{\parallel}$ field component that couples to the qubit transition.

Temperature	$\partial B_{\parallel}/\partial x$ (T/m)	$B_{\parallel}^{0}$ (μT)
300 K	20.4 ± 0.2	92.2 ± 0.4
77 K	30.7 ± 0.2	166.8 ± 0.5
21 K	39.4 ± 0.2	223.4 ± 0.9

characteristic impedance of the RF-carrying wire. The impact of the choke on the microwave reflection is small relative to that of the RF wiring and the capacitance (>1pF) of the solder pads. We estimate a ≈70% reflection of the coupled microwave power from these components. This effect can be completely mitigated in future surface traps by creating a well-defined impedance boundary for microwaves on the RF line, such that a resonance cannot be formed. Simulations show that a spiral inductor, in line with the RF electrode, and placed at a distance $\lambda/4$ from the RF electrode ends (see figures S3(b) and (c)), has the desired effect. Besides the unexpected position of the null, the measured microwave gradient per watt is approximately two times smaller than indicated in the simulations in table 2. We attribute this discrepancy to the simulation being performed for one watt input power to the trap chip, whereas gradients were measured for one watt power injected into the vacuum system as a whole.

By considering the simplified model in figure 2(b), the complex amplitude of the microwave field parallel to the static magnetic field can be approximated by

$$B_{\parallel}(x) = B_{\parallel}^{x_0} + \mathrm{e}^{\mathrm{i}\varphi}\frac{\partial B_{\parallel}}{\partial x}(x - x_0) \tag{1}$$

where $B_{\parallel}^{x_0}$ is the residual magnetic field amplitude at $x = x_0$, the position of the microwave minimum, the RF null is at $x = 0$ and φ is the phase shift between the microwave amplitude and gradient resulting from the phase difference of the opposing currents in the microwave electrode. The fitted gradients and field amplitudes at the RF null are displayed in table 4. We observe an increase in the measured field gradient as the trap temperature is reduced, consistent with the decrease in the resistivity of the gold surface layer of the trap. From a previous iteration of the surface trap, which did not suffer from resonant coupling to the RF electrode, we were able to extract the resistivity of the gold as a function of trap temperature (see section S3), and hence Q. The temperature scaling of Q is consistent with that of the measured microwave field gradient.

From the measured field gradient and field amplitude we are able to calculate an effective Lamb-Dicke parameter η at the RF null, defined as $\eta = \Omega_{\mathrm{sideband}}/\Omega_{\mathrm{carrier}} = q_0 \partial_x B_{\parallel}/B_{\parallel}^{0}$ where q_0 is the r.m.s. extent of the ion's ground-state wave packet. At 20 K and a radial secular frequency of 5.5 MHz, $\eta \approx 8 \times 10^{-4}$, which is comparable to $\eta \approx 1 \times 10^{-3}$ in our previous work [37]. If the microwave minimum were at its designed position, we would obtain $\eta \approx 3 \times 10^{-3}$. Despite not achieving an increased effective Lamb-Dicke parameter, we are able to achieve significantly faster two-qubit gates.

6.3. Measurements of ion trapping lifetimes and motional mode heating rates

One of the advantages of operating at cryogenic temperatures is an increase in ion trapping lifetime due to a reduction of background gas pressure in the UHV chamber. During room temperature operation, the UHV chamber vacuum pressure was measured with an ion gauge to be $\approx 1 \times 10^{-11}$ mbar. The approximate single- and two-ion trapping lifetimes with continuous Doppler cooling are displayed in table 5. Two-ion trapping lifetimes are expected to be shortened due to ion-ion repulsion and increased background gas collisions. However, the ion lifetimes within cryogenically operated surface traps can be significantly longer than those observed here [71]. We attribute our lifetimes, in part, to the multiple apertures which allow entry of other background gases from the room temperature region of the chamber. Further, we observe a rapid increase in ion lifetime as the temperature of the pillbox is reduced. At cryogenic temperatures, the saturation pressure of typical gases in a UHV chamber fall below 1×10^{-12} mbar [72], resulting in a reduction in local background gases near the trapped ions. The dominant source of residual background gas at 21 K is expected to be hydrogen. This could also be reduced by cooling to 4 K, but the cost of cryogen outweighs the benefits given the observed two-ion lifetime: given the same heat load, 4 K would be about an order of magnitude more expensive to maintain with a liquid helium flow cryostat.

Another advantage of cryogenic operation is the reduction in the heating rate of the motional modes of the ions. From previous experiments which have characterised ion heating rates as a function of temperature

Table 5. Approximate single-ion (τ_1) and two-ion (τ_2) trapping lifetimes with continuous Doppler cooling, as a function of surface trap temperature.

Temperature	τ_1 (minutes)	τ_2 (minutes)
300 K	≈ 30	≈ 3
77 K	> 120	≈ 20
21 K	> 600	> 120

Table 6. Measured heating rates for the single-ion in-plane radial mode $\dot{\bar{n}}_1$ and for the two-ion in-plane radial rocking mode $\dot{\bar{n}}_2$ as function of surface trap temperature.

Temperature	$\dot{\bar{n}}_1$ (quanta/s)	$\dot{\bar{n}}_2$ (quanta/s)
300 K	350 ± 50	—
77 K	230 ± 20	5.5 ± 0.7
21 K	200 ± 10	3.1 ± 0.9

[39, 42, 43, 56, 57], one would expect a power-law relationship of the type $\dot{\bar{n}} \propto T^{\beta}$, where β typically varies between 1.5 and 4 [73].

We measured the ion heating rates on the single- and two-ion radial motional modes as a function of surface trap temperature using pulsed sideband cooling [74] and sideband thermometry. These were implemented by driving the $|F = 4, m = +4\rangle \rightarrow |F = 4, m = +3\rangle$ optical Raman transition and its sidebands. The two Raman beams were derived from the same laser, detuned 30 GHz from the 397 nm $4S_{1/2} \rightarrow 4P_{1/2}$ transition, and had orthogonal linear polarisations. The beams propagated along the $(\hat{z} + \hat{x})/\sqrt{2}$ and $(\hat{z} - \hat{x})/\sqrt{2}$ directions so that there was no Raman coupling to the axial motional modes. The ions were initially Doppler cooled, after which dark-resonance cooling was applied for a further 10 ms [69]. The ions were then prepared in the $|F = 4, m = +4\rangle$ state via optical pumping with the circularly-polarised 397 nm beam. Ground-state cooling was then performed using a pulsed-sideband cooling technique which consists of a repeated sequence of driving the first red motional sideband with the Raman beams, after which the circularly-polarised 397 nm beam was used to provide dissipative repumping into the $|F = 4, m = +4\rangle$ state. Thermometry was then performed by measuring the ratio of the amplitude of the first red and blue motional Raman sidebands.

The measured heating rates for the single-ion in-plane radial mode $\dot{\bar{n}}_1$ and the two-ion in-plane radial rocking mode $\dot{\bar{n}}_2$ are shown in table 6. The mode of most interest is the two-ion in-plane radial rocking mode, as this is the mode on which two-qubit entangling gates are to be performed. From a conservative $\dot{\bar{n}} \propto T^{\beta=1.5}$ scaling law we would have expected a $\sim 54\times$ heating rate reduction between room temperature and 21 K [39, 42, 43, 56, 57]. However, we only observe a $1.5\times$ reduction in heating. This is a much smaller effect than one would expect from previous cryogenic experiments, and may indicate that the electric field noise arises from technical sources which are currently unidentified. Typical sources for such noise include noisy electronics and ground loops.

7. Conclusions

In this paper we have presented a novel surface-electrode ion trap with an integrated microwave resonator, designed to improve upon the speed and fidelity of two-qubit entangling operations presented in our previous work [37]. One of the main aims was to increase the achievable microwave-frequency magnetic field gradient for a given input power, whilst maintaining or improving upon the effective Lamb-Dicke parameter η and motional-mode heating rate. With the use of a passively-nulled resonant microwave electrode design and a π-polarized qubit transition that couples more efficiently to the microwave field, we have obtained a microwave field gradient which is effectively a factor of eight greater than that of our previous system, for the same input power. This should enable an order-of-magnitude improvement in the speed of two-qubit entangling operations for reasonable input microwave powers [75].

We have observed a detrimental resonant coupling between the microwave and RF electrodes, which does not affect the achievable gradient, but causes a shift in the position of the microwave field minimum, which in turn reduces η; however, the measured η is comparable to that of our previous work. We have shown in simulation that this resonant coupling between the microwave and RF electrodes could be mitigated by placement of an inductive choke on the RF electrode at a distance $\lambda/4$ from the microwave resonator.

The ability to cool the surface trap to cryogenic temperatures has yielded ion trapping lifetimes of several hours. In addition, we have observed a reduction in motional heating rates at cryogenic temperatures, which has enabled us to maintain a comparable motional heating rate to that in our previous system, despite the

significantly reduced ion-to-electrode distance. Future work will utilise these improvements to demonstrate microwave-driven two-qubit entangling operations which are comparable in both speed and fidelity to those of state-of-the-art laser-driven gates.

Data availability statement

The data that support the findings of this study are openly available at the following URL/DOI: https://ora.ox.ac.uk/objects/uuid:eb110766-2e81-4680-a680-d17afa3513c7.

Acknowledgments

We thank members of the NIST Ion Storage group, in particular David Allcock and Raghu Srinivas, for much helpful advice on cryogenic ion trap design and operation. TPH would like to thank NIST for their hospitality during an extended visit. We acknowledge the helpful work of Dr Paul Gow and Dr James Gates (at Southampton U.). C J B and T P H are Directors of Oxford Ionics Ltd This work was supported by the U.S. Army Research Office (reference W911NF-18-1-0340) and the U.K. EPSRC Quantum Computing and Simulation Hub.

ORCID iDs

M A Weber https://orcid.org/0000-0001-6603-4885
J Wolf https://orcid.org/0009-0005-5378-4288
M F Gely https://orcid.org/0000-0002-2861-2709
R K Hanley https://orcid.org/0000-0001-8373-1025
J F Goodwin https://orcid.org/0000-0001-5656-2086
C J Ballance https://orcid.org/0000-0002-9654-9510
T P Harty https://orcid.org/0000-0003-4077-226X

References

[1] Harty T P, Allcock D T C, Ballance C J, Guidoni L, Janacek H A, Linke N M, Stacey D N and Lucas D M 2014 High-fidelity preparation, gates, memory and readout of a trapped-ion quantum bit *Phys. Rev. Lett.* **113** 220501
[2] Gaebler J P *et al* 2016 High-fidelity universal gate set for be $^{9}Be^{+}$ ion qubits *Phys. Rev. Lett.* **117** 060505
[3] Ballance C J, Harty T P, Linke N M, Sepiol M A and Lucas D M 2016 High-fidelity quantum logic gates using trapped-ion hyperfine qubits *Phys. Rev. Lett.* **117** 060504
[4] Srinivas R *et al* 2021 High-fidelity laser-free universal control of trapped ion qubits *Nature* **597** 209–13
[5] Clark C R *et al* 2021 High-fidelity bell-state preparation with $^{40}Ca^{+}$ optical qubits *Phys. Rev. Lett.* **127** 130505
[6] Gottesman D 1998 Theory of fault-tolerant quantum computation *Phys. Rev.* A **57** 127
[7] Raussendorf R and Harrington J 2007 Fault-tolerant quantum computation with high threshold in two dimensions *Phys. Rev. Lett.* **98** 190504
[8] Langer C *et al* 2005 Long-lived qubit memory using atomic ions *Phys. Rev. Lett.* **95** 060502
[9] Häffner H *et al* 2005 Robust entanglement *App. Phys.* B **81** 151–3
[10] Sepiol M A, Hughes A C, Tarlton J E, Nadlinger D P, Ballance T G, Ballance C J, Harty T P, Steane A M, Goodwin J F and Lucas D M 2019 Probing qubit memory errors at the part-per-million level *Phys. Rev. Lett.* **123** 110503
[11] Wang Y, Um M, Zhang J, An S, Lyu M, Zhang J-N, Duan L-M, Yum D and Kim K 2017 Single-qubit quantum memory exceeding ten-minute coherence time *Nat. Photon.* **11** 646–50
[12] Nägerl H C, Roos C, Leibfried D, Rohde H, Thalhammer G, Eschner J, Schmidt-Kaler F and Blatt R 2000 Investigating a qubit candidate: spectroscopy on the $S_{1/2}$ to $D_{5/2}$ transition of a trapped calcium ion in a linear Paul trap *Phys. Rev.* A **61** 023405
[13] Monroe C, Meekhof D M, King B E, Itano W M and Wineland D J 1995 Demonstration of a fundamental quantum logic gate *Phys. Rev. Lett.* **75** 4714
[14] Nägerl H C, Leibfried D, Rohde H, Thalhammer G, Eschner J, Schmidt-Kaler F and Blatt R 1999 Laser addressing of individual ions in a linear ion trap *Phys. Rev.* A **60** 145
[15] Wineland D J, Monroe C, Itano W M, Leibfried D, King B E and Meekhof D M 1998 Experimental issues in coherent quantum-state manipulation of trapped atomic ions *J. Res. Natl Inst. Stan.* **103** 259
[16] Ozeri R *et al* 2007 Errors in trapped-ion quantum gates due to spontaneous photon scattering *Phys. Rev.* A **75** 042329
[17] Schäfer V M, Ballance C J, Thirumalai K, Stephenson L J, Ballance T G, Steane A M and Lucas D M 2018 Fast quantum logic gates with trapped-ion qubits *Nature* **555** 75–78
[18] Moore I D, Campbell W C, Hudson E R, Boguslawski M J, Wineland D J and Allcock D T C 2023 Photon scattering errors during stimulated raman transitions in trapped-ion qubits *Phys. Rev.* A **107** 032413
[19] Leu A D, Gely M F, Weber M A, Smith M C, Nadlinger D P, and Lucas D M 2023 Fast, high-fidelity addressed single-qubit gates using efficient composite pulse sequences (arXiv:2305.06725)
[20] Mintert F and Wunderlich C 2001 Ion-trap quantum logic using long-wavelength radiation *Phys. Rev. Lett.* **87** 257904
[21] Johanning M, Varón A F and Wunderlich C 2009 Quantum simulations with cold trapped ions *J. Phys. B: At. Mol. Opt.* **42** 154009
[22] Lake K, Weidt S, Randall J, Standing E D, Webster S C and Hensinger W K 2015 Generation of spin-motion entanglement in a trapped ion using long-wavelength radiation *Phys. Rev.* A **91** 012319
[23] Webster S C, Weidt S, Lake K, McLoughlin J J and Hensinger W K 2013 Simple manipulation of a microwave dressed-state ion qubit *Phys. Rev. Lett.* **111** 140501

[24] Mikelsons G, Cohen I, Retzker A and Plenio M B 2015 Universal set of gates for microwave dressed-state quantum computing *New J. Phys.* **17** 053032
[25] Cohen I, Weidt S, Hensinger W K and Retzker A 2015 Multi-qubit gate with trapped ions for microwave and laser-based implementation *New J. Phys.* **17** 043008
[26] Ospelkaus C, Langer C E, Amini J M, Brown K R, Leibfried D and Wineland D J 2008 Trapped-ion quantum logic gates based on oscillating magnetic fields *Phys. Rev. Lett.* **101** 090502
[27] Ospelkaus C, Warring U, Colombe Y, Brown K R, Amini J M, Leibfried D and Wineland D J 2011 Microwave quantum logic gates for trapped ions *Nature* **476** 181–4
[28] Srinivas R, Burd S C, Sutherland R T, Wilson A C, Wineland D J, Leibfried D, Allcock D T C and Slichter D H 2019 Trapped-ion spin-motion coupling with microwaves and a near-motional oscillating magnetic field gradient *Phys. Rev. Lett.* **122** 163201
[29] Kielpinski D, Monroe C and Wineland D J 2002 Architecture for a large-scale ion-trap quantum computer *Nature* **417** 709–11
[30] Mc Hugh D and Twamley J 2005 Quantum computer using a trapped-ion spin molecule and microwave radiation *Phys. Rev.* A **71** 012315
[31] Chiaverini J and Lybarger W E 2008 Laserless trapped-ion quantum simulations without spontaneous scattering using microtrap arrays *Phys. Rev.* A **77** 022324
[32] Monroe C and Kim J 2013 Scaling the ion trap quantum processor *Science* **339** 1164–9
[33] Allcock D T C, Harty T P, Ballance C J, Keitch B C, Linke N M, Stacey D N and Lucas D M 2013 A microfabricated ion trap with integrated microwave circuitry *Appl. Phys. Lett.* **102** 044103
[34] Carsjens M, Kohnen M, Dubielzig T and Ospelkaus C 2013 Surface-electrode Paul trap with optimized near-field microwave control *Appl. Phys.* B **114** 243–50
[35] Bautista-Salvador A, Zarantonello G, Hahn H, Preciado-Grijalva A, Morgner J, Wahnschaffe M and Ospelkaus C 2019 Multilayer ion trap technology for scalable quantum computing and quantum simulation *New J. Phys.* **21** 043011
[36] Hahn H, Zarantonello G, Bautista-Salvador A, Wahnschaffe M, Kohnen M, Schoebel J, Schmidt P O and Ospelkaus C 2019 Multilayer ion trap with three-dimensional microwave circuitry for scalable quantum logic applications *Appl. Phys.* B **125** 154
[37] Harty T P, Sepiol M A, Allcock D T C, Ballance C J, Tarlton J E and Lucas D M 2016 High-fidelity trapped-ion quantum logic using near-field microwaves *Phys. Rev. Lett.* **117** 140501
[38] Zarantonello G, Hahn H, Morgner J, Schulte M, Bautista-Salvador A, Werner R F, Hammerer K and Ospelkaus C 2019 Robust and resource-efficient microwave near-field entangling Be+ 9 gate *Phys. Rev. Lett.* **123** 260503
[39] Deslauriers L, Olmschenk S, Stick D, Hensinger W K, Sterk J and Monroe C 2006 Scaling and suppression of anomalous heating in ion traps *Phys. Rev. Lett.* **97** 103007
[40] Sedlacek J A, Greene A, Stuart J, McConnell R, Bruzewicz C D, Sage J M and Chiaverini J 2018 Distance scaling of electric-field noise in a surface-electrode ion trap *Phys. Rev.* A **97** 020302
[41] Brownnutt M, Kumph M, Rabl P and Blatt R 2015 Ion-trap measurements of electric-field noise near surfaces *Rev. Mod. Phys.* **87** 1419–82
[42] Labaziewicz J, Ge Y, Antohi P, Leibrandt D, Brown K R and Chuang I L 2008 Suppression of heating rates in cryogenic surface-electrode ion traps *Phys. Rev. Lett.* **100** 013001
[43] Chiaverini J and Sage J M 2014 Insensitivity of the rate of ion motional heating to trap-electrode material over a large temperature range *Phys. Rev.* A **89** 012318
[44] Wahnschaffe M, Hahn H, Zarantonello G, Dubielzig T, Grondkowski S, Bautista-Salvador A, Kohnen M and Ospelkaus C 2017 Single-ion microwave near-field quantum sensor *Appl. Phys. Lett.* **110** 034103
[45] Pozar D M 2011 *Microwave Engineering* (Wiley)
[46] ANSYS Inc. ANSYS® HFSS v. 17.0
[47] COMSOL Inc. COMSOL Multiphysics® v. 5.4
[48] Ion Storage Group (NIST), private communication
[49] Mølmer K and Sørensen A 1999 Multiparticle entanglement of hot trapped ions *Phys. Rev. Lett.* **82** 1835
[50] Sørensen A and Mølmer K 1999 Quantum computation with ions in thermal motion *Phys. Rev. Lett.* **82** 1971
[51] Allen Matula R 1979 Electrical resistivity of copper, gold, palladium and silver *J. Phys. Chem. Ref. Data* **8** 1147–298
[52] Martinez W E, Gregori G and Mates T 2010 Titanium diffusion in gold thin films *Thin Solid Films* **518** 2585–91
[53] Li D, Shang Z, She Y and Wen Z 2017 Investigation of Au/Si eutectic wafer bonding for MEMS accelerometers *Micromachines* **8** 158
[54] Wolf J 2019 Cryogenic, near-field quantum logic chips with passive field nulling on $^{43}Ca^{+}$ *PhD Thesis* Oxford University
[55] P/N: 110797, Accu-Glass Products, Inc.
[56] Daniilidis N, Narayanan S, Möller S A, Clark R, Lee T E, Leek P J, Wallraff A, Schulz S, Schmidt-Kaler F and Häffner H 2011 Fabrication and heating rate study of microscopic surface electrode ion traps *New J. Phys.* **13** 013032
[57] Noel C, Berlin-Udi M, Matthiesen C, Yu J, Zhou Y, Lordi V and Häffner H 2019 Electric-field noise from thermally activated fluctuators in a surface ion trap *Phys. Rev.* A **99** 063427
[58] Diederich M, Häffner H, Hermanspahn N, Immel M, Kluge H J, Ley R, Mann R, Quint W, Stahl S and Werth G 1998 Observing a single hydrogen-like ion in a penning trap at T = 4 K *Hyperfine Interact.* **115** 185–92
[59] Pagano G *et al* 2018 Cryogenic trapped-ion system for large scale quantum simulation *Quantum Sci. Technol.* **4** 014004
[60] Ballance T G, Goodwin J F, Nichol B, Stephenson L J, Ballance C J and Lucas D M 2018 A short response time atomic source for trapped ion experiments *Rev. Sci. Instrum.* **89** 053102
[61] Matijasevic G S, Lee C C and Wang C Y 1993 Au-Sn alloy phase diagram and properties related to its use as a bonding medium *Thin Solid Films* **223** 276–87
[62] DT-670-SD-1.4L Lakeshore Electronics.
[63] Thermotive LLC
[64] Teufel J D, Li D, Allman M S, Cicak K, Sirois A J, Whittaker J D and Simmonds R W 2011 Circuit cavity electromechanics in the strong-coupling regime *Nature* **471** 204–8
[65] One would expect a small change in coupling, on the order of a few percent, due to a change in dielectric constant of the sapphire substrate; however this is negligible compared to the change in resistive losses of the resonator
[66] Molla J, Ibarra A, Margineda J, Zamarro J M and Hernandez A 1993 Dielectric property measurement system at cryogenic temperature and microwave frequencies *IEEE Trans. Instrum. Meas.* **42** 817–21
[67] Lucas D M, Ramos A, Home J P, McDonnell M J, Nakayama S, Stacey J-P, Webster S C, Stacey D N and Steane A M 2004 Isotope-selective photoionization for calcium ion trapping *Phys. Rev.* A **69** 012711
[68] Bourdeauducq S *et al* m-labs/artiq: 6.0, 2018

[69] Allcock D T C, Harty T P, Sepiol M A, Janacek H A, Ballance C J, Steane A M, Lucas D M and Stacey D N 2016 Dark-resonance Doppler cooling and high fluorescence in trapped Ca-43 ions at intermediate magnetic field *New J. Phys.* **18** 023043
[70] Myerson A H, Szwer D J, Webster S C, Allcock D T C, Curtis M J, Imreh G, Sherman J A, Stacey D N, Steane A M and Lucas D M 2008 High-fidelity readout of trapped-ion qubits *Phys. Rev. Lett.* **100** 200502
[71] Dubielzig T, Halama S, Hahn H, Zarantonello G, Niemann M, Bautista-Salvador A and Ospelkaus C 2021 Ultra-low-vibration closed-cycle cryogenic surface-electrode ion trap apparatus *Rev. Sci. Instrum.* **92** 043201
[72] Honig R E and Hook H O 1960 Vapor pressure data for some common gases *RCA Rev.* **21** 360–8
[73] Labaziewicz J, Ge Y, Leibrandt D R, Wang S X, Shewmon R and Chuang I L 2008 Temperature dependence of electric field noise above gold surfaces *Phys. Rev. Lett.* **101** 180602
[74] Monroe C, Meekhof D M, King B E, Jefferts S R, Itano W M, Wineland D J and Gould P 1995 Resolved-sideband raman cooling of a bound atom to the 3D zero-point energy *Phys. Rev. Lett.* **75** 4011
[75] Microwave input power of a few Watts is easily generated; the trap chip has been tested for powers up to 16 W without damage.